Electronic Structure of IrO$_2$: The Role of the Metal d Orbitals

Yuan Ping,*[†,‡] Giulia Galli,[§] and William A. Goddard, III*[∥]

[†]Joint Center for Artificial Photosynthesis, Lawrence Berkeley National Laboratory, Berkeley, California 94720, United States
[‡]California Institute of Technology, Pasadena, California 91125, United States
[§]Institute for Molecular Engineering, The University of Chicago, 5801 South Ellis Avenue, Chicago, Illinois 60637, United States
[∥]Materials and Process Simulation Center, California Institute of Technology, Pasadena, California 91125, United States

S *Supporting Information*

ABSTRACT: IrO$_2$ is one of the most active catalysts for the oxygen evolution reaction (OER) and remains the only known stable OER catalyst in acidic conditions. As a first step in understanding the mechanism for OER we carried out detailed Density Functional Theory (DFT) studies of the electronic structure of IrO$_2$. We compared the electronic states and magnetic properties of IrO$_2$ using several density functionals. We found that DFT with hybrid functionals (B3PW and PBE0) leads to a weak ferromagnetic coupling, although IrO$_2$ has often been reported as nonmagnetic. We also found a magnetic ground state for RuO$_2$, whose electronic structure is similar to that of IrO$_2$. Ru–Ru antiferromagnetic interaction has been observed experimentally in nanoparticle RuO$_2$. Further low temperature measurements are necessary to confirm whether a weak magnetism may occur below 20 K in IrO$_2$. We also found that PBE leads to a better agreement with the experimental XPS spectra, compared with hybrid functionals and PBE+U.
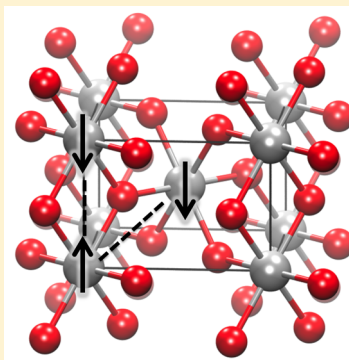
INTRODUCTION

A critical area of research for renewable energy is the development of improved materials effective for electrochemical and photoelectrochemical water splitting and production of H$_2$ and O$_2$. Currently, the only known oxygen evolution reaction(OER) catalyst stable in acidic condition is IrO$_2$ and it exhibits high catalytic activity for the OER.[1,2] However, the detailed atomistic reaction mechanism leading to high levels of O$_2$ evolution remains unclear, making it difficult to search for other less expensive OER candidates. As a first step in determining this mechanism, we used density functional theory (DFT) to study the electronic properties of IrO$_2$. In addition to being an efficient catalyst for water splitting, IrO$_2$ is the only known catalyst capable of producing O$_2$ in acidic conditions for the H$_2$O oxidation half reaction combined with CO$_2$ reduction. Photoelectrochemical measurements are usually carried out in acidic or basic conditions because a photoelectrochemical cell operating at neutral pH conditions suffers from the overpotential losses associated with local pH changes at the active sites as well as from the possible formation of a bulk pH gradient.[1]

In another research area, iridates (e.g., Sr$_2$IrO$_4$,[3,4] BaIrO$_3$,[5−7] Sr$_3$Ir$_2$O$_7$[8]), where Ir has the same formal charge as in IrO$_2$, have drawn significant interest in recent years because many of them are magnetic insulators with exotic electronic and magnetic properties.[3−8] In contrast, IrO$_2$ is a metal usually considered to be in a paramagnetic state.

Previous DFT studies of IrO$_2$ have been limited to the local density approximation (LDA) and generalized gradient approximations (GGA), e.g. PBE or PBEsol.[9−11] It is well-

known that for semiconductors or insulators, these approximations often lead to substantial errors for the band structure, for example, band gaps that are too small, compared to experiments, sometimes even zero. This problem has been discussed in depth in the past and traced to the delocalization error (many approximate functionals exhibit a convex behavior in violation of the linearity condition for fractional charges).[12,13] For semiconductors or insulators, hybrid[14−16] and screened hybrid functionals[17] have demonstrated significant improvement for band structures and band gaps over LDA or GGA.[18] However, major challenges still remain, and there is no functional capable of predicting accurate band structures for all classes of materials including metal, semiconductor, and large band gap insulators. Since IrO$_2$ is a metallic oxide, it is not straightforward to predict whether semilocal functionals (e.g.PBE) or hybrid functionals (e.g., B3PW91) would perform better for its electronic and magnetic properties. In particular, the electronic structure of IrO$_2$, with d orbitals that might localize but also participate in bonding, makes it dramatically different from normal metals.

Although IrO$_2$ bonds have considerable covalent character, it is a reasonable approximation to consider the O atoms as O^{2-} and the Ir atom as Ir^{4+}. This leaves 5d electrons on the Ir, where the strong octahedral ligand field stabilizes the three t_{2g} orbitals, which have nodal planes through the polar Ir−O bonds. This leads to two doubly occupied t_{2g} orbitals and one

singly occupied orbital leaving each Ir with one unpaired spin. Thus, one expects a very narrow partially filled t_{2g} band that might lead to ferro- or antiferromagnetic coupling depending on the overlap of these t_{2g} orbitals. However, experiments have generally reported IrO_2 to be a paramagnetic material,[19] indicating that the interaction of t_{2g} orbitals on neighboring atoms is small.

In this paper we compare various levels of DFT theory, including GGA (PBE), Hubbard U corrected PBE (PBE+U), and hybrid functionals (B3PW91 and PBE0), and we address whether weak magnetism may be present in metallic IrO_2.

■ COMPUTATIONAL DETAILS

For the PBE and PBE+U calculations, we used the Quantum Espresso package,[20] with ultrasoft small core pseudopotentials[21] where the eight outer core (5s, 5p) electrons of Ir were described explicitly along with the nine valence electrons. A kinetic energy cutoff of 40 Ry for the wave function and of 240 Ry for the density together with a $(10 \times 10 \times 12)$ Monkhorst−Pack k-point grid were used in geometry optimization; a $(12 \times 12 \times 16)$ k-point grid was instead used for density of states calculations. Since IrO_2 is a metal, we applied the Marzari-Vanderbilt cold smearing[22] of 0.02 Ry to the computed eigenvalues so as to improve the k-point convergence of our calculations.

The calculations with the hybrid functionals B3PW91[14] and PBE0[15] were performed using the CRYSTAL09 code and angular momentum projected core effective potentials (Hay-Wadt)[23] to replace the deeper core electrons of Ir (also small core describing explicitly the eight 5s, 5p core electrons plus the nine valence electrons); we used a triple-ζ split-valence plus polarization basis set for Ir[24] atoms and double-ζ split-valence basis set for Ru[23,25] and O[26] atoms. All electrons were included for the O atom. We used a very fine k-point mesh $(16 \times 16 \times 16)$ to diagonalize KS/Fock matrix and $(32 \times 32 \times 32)$ k points to compute the Fermi energy and density matrix with zero smearing, in order to obtain accurate total energies for magnetic calculations (total energies are converged with k-point mesh within 0.1 meV per atom). Detailed information on our calculations is given in the Supporting Information (SI), including the basis sets, the comparison of the structural and electronic properties, and phonon frequencies of IrO_2 obtained with the Quantum Espresso package and the Crystal code. The purpose of these comparisons is to show that the results for PBE using atomic basis sets in CRYSTAL agree well with the results using PBE with plane waves. This establishes that the accuracy of our results is not affected by basis sets or the choice of other numerical parameters. In particular, we showed that the band structures computed at the same experimental structure by the two codes (Figure S1) are nearly identical, especially for the bands close to the Fermi level and the valence bands; larger errors (0.1−0.5 eV) appear in higher unoccupied bands, which is however not a concern here since, in this paper, we focus on ground state properties. We also compared the optimized lattice constants and internal geometry and showed the lattice constants (internal geometry) differed by 0.50% (0.13%) when computed with the two codes (as shown in Table S1). We also compared the phonon frequencies computed by two codes, as shown in Table S2. We found satisfactory agreement within 2−20 cm^{-1}.

At ambient conditions IrO_2 adopts a rutile (tetragonal) structure with measured lattice constants a = 8.513 bohr and c = 5.969 bohr. The calculated PBE lattice constants at 0 K are

0.7% larger and the error on the internal geometry is 0.06% compared to experiments at 300 K.[27] Since the magnetic properties are very sensitive to the structure and the spin coupling constant is of the order of meV, we used the experimental structure to study the electronic structure of IrO_2. We note that it is common to use the experimental structure for the study of magnetic properties of complex oxides.[28,29] On the other hand, we found the electronic levels changed by less than 50 meV at the experimental and optimized structures when using PBE and B3PW91.

■ ELECTRONIC STRUCTURE OF IRO$_2$ AT VARIOUS LEVELS OF THEORY

DFT Description of the Electronic Structure of IrO_2. At ambient conditions, the rutile structure of IrO_2 (see Figure 1)
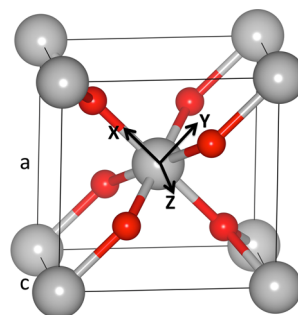

Figure 1. Ball and stick representation of the crystal structure of rutile IrO_2 (The unit cell is shown). The lattice parameter c is along the z axis, and the y axis bisects the O−Ir−O 104° angle in the plane formed by the metal and the four oxygens. Thus, d_{xz}, d_{xy}, and $d_{y^2-z^2}$ orbitals are π-like t_{2g} orbitals, while d_{x^2} and d_{yz} are σ-like e_g orbitals. The fully occupied $d_{y^2-z^2}$ orbital has the lowest energy. The d_{xy} interacts with the doubly occupied p_y orbital on the oxygens in the $\pm x$ direction, stabilizing the p_y while destabilizing d_{xy}. This pushes d_{xy} above d_{xz}, making d_{xz} doubly occupied and d_{xy} singly occupied.

has two formula per tetragonal unit cell. Each Ir is bonded to six O atoms in a slightly distorted octahedral environment, while each O is bonded to three Ir in a distorted planar trigonal arrangement. This leads to four long (2.00 Å) and two short (1.96 Å) Ir−O σ bonds, with O−Ir−O angles of 104.4/75.6° in the yz plane of the crystal structure. The projected density of states (PDOS) of IrO_2 in Figure 2a shows that the bonding combinations of O $2p_\sigma$ orbitals hybridized with Ir e_g lies below −7.5 eV. This leaves five electrons to distribute among the three t_{2g} orbitals which have nodal planes through the Ir−O bonds; these orbitals contribute weakly to the bonding π
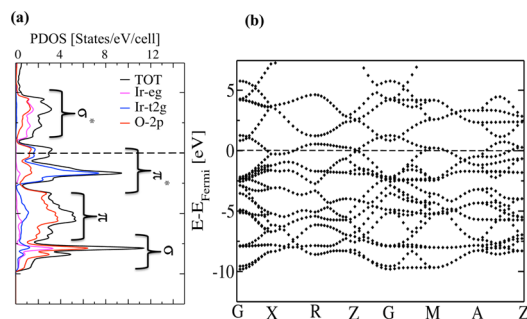

Figure 2. Band structure of IrO_2 computed at the PBE level of theory (left) and projected density of states (right).

orbitals between -7.5 to -2.5 eV, by hybridizing with the O $2p_\pi$ orbitals perpendicular to the O−Ir bonds. The t_{2g} orbitals dominate the antibonding π orbitals between -2.5 and 1 eV above the Fermi level. With the t_{2g} band only 5/6 filled, the Fermi level is expected to cross near the top of the t_{2g} band, making IrO_2 metallic. Indeed, the computed PBE band structure of IrO_2, displayed in Figure 2b, shows the Fermi level crossing the t_{2g} bands of Ir, confirming the metallic character of IrO_2, consistent with previous PBE studies.[9−11]

Since the Fermi level crosses the t_{2g} orbitals, the population of these orbitals determines the electronic structure of IrO_2. Figure 3a displays the PDOS of the t_{2g} orbitals for the center Ir
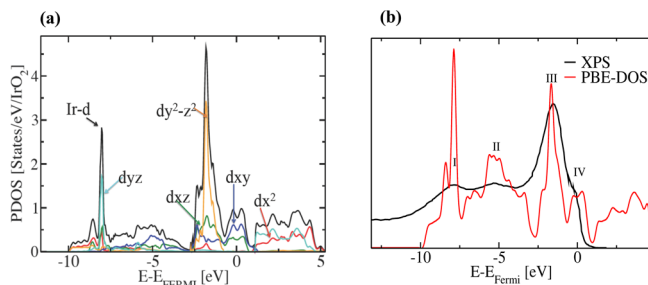

Figure 3. Projected density of states (PDOS) of the 5d states of the central Ir atom of Figure 1 computed at the PBE level of theory(left). The green and dark blue curves represent d_{xz} and d_{xy} orbitals, respectively; the light blue curve represents the d_{yz} orbital, and the red and orange curves represent the d_{x^2} and $d_{y^2-z^2}$ orbitals, respectively. The density of states computed within PBE is compared with the experimental XPS spectrum on the right-hand side.

atom shown in Figure 1, where the (x,y,z) axes are defined. In this coordinate system, the three t_{2g} orbitals have d_{xz}, d_{xy}, and $d_{y^2-z^2}$ character (each of which is π-like with respect to the Ir−O bonds) and the e_g orbitals (σ like) become d_{x^2} and d_{yz}. The $d_{y^2-z^2}$ orbital is the most stable and it is fully occupied; d_{xz} is also doubly occupied. Here d_{xy} couples with the doubly occupied p_y orbitals of the O atoms in the $\pm x$ directions, stabilizing the p_y, while destabilizing d_{xy}. For the other Ir atom in the unit cell, the x and y axes are switched by symmetry. Hence, the singly occupied d orbital on one Ir is orthogonal to the singly occupied d orbital on the other Ir in the unit cell, which we expected to lead to very weak ferromagnetic coupling. Indeed, as discussed below, we find that the hybrid DFT calculations lead to a ferromagnetic ground state with a Curie temperature of either 20 K (B3PW91) or 32 K (PBE0). In contrast, including spin optimization at the PBE level always led to a nonmagnetic ground state.

We now turn to the discussion of spin orbit coupling. In the simple bonding description given above, the degeneracy among the three occupied t_{2g} orbitals is lifted (with single particle orbital energies: $d_{y^2-z^2} < d_{xz} < d_{xy}$) so that there are no first order spin−orbit effects. We performed scalar relativistic calculations of IrO_2 and compared with full relativistic

calculation by including spin−orbit coupling explicitly only for Ir. The spin−orbit splitting gives <0.2 eV shift of the states around -2 eV, corresponding to the energy of the t_{2g} orbital($d_{y^2-z^2}$). In other parts of the spectrum, spin−orbit coupling makes minimal contributions. Hence, in IrO_2 spin−orbit interaction did not give rise to a splitting of the bands at the Fermi level so as to form a finite band gap, unlike in other insulating iridates.[4] Similar results have been obtained in ref 11 as well.

We compared our computed DOS with the experimental XPS spectra, as shown in Figure 3b. We do not expect a perfect agreement between theory and experiments because we did not include the matrix element effects, as was done in ref 11. However, we expect the peak positions between the XPS spectra and the DOS computed at the appropriate level of theory should be aligned, as discussed in refs 30 and 31. Interestingly, we see clearly that the peak positions of XPS are close to the DOS computed by PBE, where we aligned the two curves by their corresponding Fermi levels. Similar results were reported in ref 11, which used the PBE-sol functional and compared calculations with experimental hard X-ray photoemission spectra.

Since the Ir atoms have five electrons in d orbitals, we expected the standard DFT delocalization error to be non-negligible in IrO_2. For transition metal oxides with partially filled d states, two methods are often used to overcome DFT errors: one is to apply Hubbard U corrections to the metal d states, thus, increasing the on-site d electron Coulomb interaction (as discussed in DFT+U Description of the Electronic Structure of IrO_2); the other method is to use hybrid functionals (e.g., B3PW91 or PBE0) with a finite amount (20−25%) of exact exchange (EXX). We note that the B3PW91 hybrid functional leads to an mean absolute error of 0.09 eV of the band gaps over 35 binary and ternary semiconductors.[18] To understand the dependence of the results on the amount of EXX, we have also computed the electronic structure of IrO_2 using B3PW91 and PBE0 (as discussed in Electronic Structure of IrO_2 Using Hybrid Functionals).

DFT+U Description of the Electronic Structure of IrO_2. In DFT+U calculations, the on-site interaction U is usually fitted to an experimental quantity of interest, for example the band gap or the magnetic moments. In this section, we considered U values ranging from 0 to 8 eV, which covers the range of nearly all DFT+U calculations for transition metal oxides. We used the simplified rotational-invariant formulation[32] implemented in the Quantum Espresso package.[20] We found that when increasing U from 0 to 8 eV, the magnetization of each Ir atom remained equal to zero.

To further confirm whether a magnetic ordering may occur, we also carried out calculations with fixed magnetic moments at both PBE (U = 0 eV) and PBE+U (U = 2, 8 eV) levels of theory. As shown in Table 1, the total energy increases

Table 1. Total Energy/Unit Cell (E; Referred to the Total Energy of the Nonmagnetic Configuration) of IrO_2 Computed with Fixed Magnetic Moments (M) per Unit Cell, at the PBE and PBE+U Levels of Theory[A]

M (μ_B)	0	2	4	6	8	10
E (Ry; U = 0)	0	0.0266	0.1913	0.4275	0.7130	1.0613
E (Ry; U = 2)	0	0.0231	0.1979	0.4421	0.7137	1.0487
E (Ry; U = 8)	0	0.0181	0.2188	0.4333	0.7510	1.0097

[A]Calculations for three values of the parameter U (0, 2, and 8 eV) are shown.

systematically with increasing the magnetic moments (from the low spin configuration with a magnetic moment of 2 μ_B to the high spin configuration with a magnetic moment of 10 μ_B for the unit cell). These results hold both at PBE and PBE+U level of theory and indicate that there is no optimal magnetization at which the system has a lower total energy than the nonmagnetic configuration.

Figure 4a shows the PDOS of IrO$_2$ computed within PBE+U, compared with experimental results (Figure 4b). By applying U
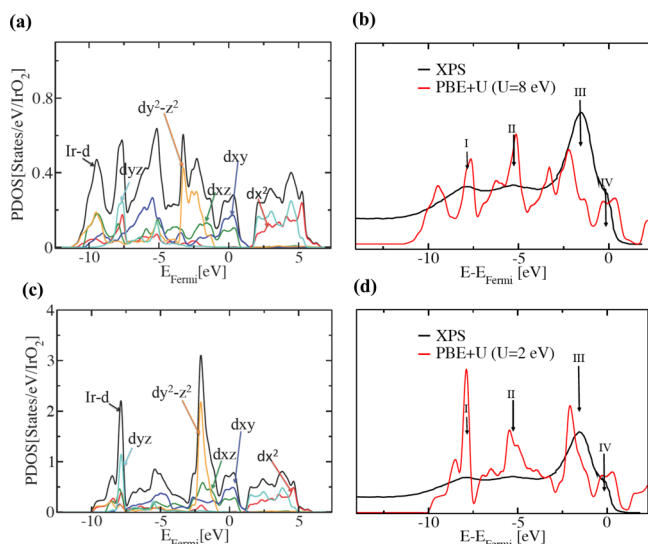

Figure 4. Projected density of states (PDOS) of the 5d states of the central Ir atom of Figure 1 computed at the PBE+U level of theory with U(Ir) = 8 eV (up left). The green and dark blue curves represent d_{xz} and d_{yx} orbitals, respectively; the light blue curve represents the d_{yz} orbital, and the red and orange curves represent the d_{x^2} and $d_{y^2-z^2}$ orbitals, respectively. The density of states computed within PBE+U (U(Ir) = 8 eV) is compared with the experimental XPS spectrum on the up right-hand side. The bottom left and right figures are the corresponding ones with U(Ir) = 2 eV.

= 8 eV (which is for the strongly correlated limit) to Ir d states, the DOS for the weakly antibonding t_{2g} levels (located between the Fermi level and −2.5 eV) is lower in intensity than that obtained with PBE; instead, the DOS at lower energies (9.5 eV below the Fermi level), which mainly arises from t_{2g} (d_{xz} and $d_{y^2-z^2}$) bonding orbitals, is higher in intensity than in the PBE case. Compared with the experimental XPS spectra (Figure 4b), peak III (around −1.6 eV, mainly composed of the $d_{y^2-z^2}$ orbital) is shifted to more negative energy by 0.7 eV while an extra peak at −9.5 eV appears (as discussed above), which is inconsistent with the experimental XPS measurements. However, 5d electrons in IrO$_2$ are not as strongly correlated as 3d electrons because of the much larger spatial extension of 5d orbitals. A value of U smaller than the strongly correlated limit (8 eV) is likely more appropriate to use for IrO$_2$. In previous DFT+U calculations of iridates, a value of U(Ir) between 0.5 to 2 eV has been applied,[3,4] which gave electronic and magnetic properties in agreement with experiments. Therefore, we also computed the PDOS and DOS of IrO$_2$ with U = 2 eV as shown in Figure 4c,d. The computed PDOS at U = 2 eV is very similar to the one computed using PBE. On the other hand, the computed DOS (in Figure 4d) shows that the peak located around −2.5 eV is still noticeably shifted to lower energy compared with the experimental XPS and PBE

results. Overall, the use of PBE+U did not improve the agreement with experimental XPS measurements, compared with PBE, indicating that the on-site Coulomb interaction U is rather small compared with the bandwidth of bulk IrO$_2$.

Electronic Structure of IrO$_2$ Using Hybrid Functionals. We performed spin-polarized calculations with the B3PW91 functional by using the CRYSTAL09 code.[33] In order to allow for the description of complex spin couplings, we examined several magnetic configurations, shown in Table 2, with a 2 × 2

Table 2. Relative Energies (ΔE) between Various Spin Configurations of IrO$_2$ Computed with a 2 × 2 × 2 Supercell with Two Different Hybrid Functionals (B3PW91 and PBE0)[a]

Configuration		Energy Component	ΔE (mHartree)	
First layer	Second layer		B3PW91	PBE0
(1)		$-32J_1-16J_2$	0	0
(2)		$32J_1-16J_2$	−0.313	7.081
(3)		$-16J_2$	−13.074	−6.515
(4)		$+16J_2$	−.0809	−1.140

[a]The energy components for each spin configuration are based on the formula discussed in the main text. Two different hybrid functionals (B3PW91 and PBE0) were used.

Table 3. Total Energy Differences (meV) between Ferromagnetic and Nonmagnetic (FM-NM) States of IrO$_2$ (for a Unit Cell with Two IrO$_2$ Formula)[a]

theory	FM-NM	J_1	J_2	spin (FM)
PBE	463			0
B3PW91	−225	−0.13	11.04	0.519
PBE0	−421	3.01	4.57	0.587

[a]We reported various spin coupling constants J; we also report the unpaired spin between spin up and spin down density for the ferromagnetic configuration per Ir atom.

× 2 supercell. As shown in Tables 2 and 3, ferromagnetic states have an energy 0.3−44.0 meV per unit cell (two IrO$_2$ formula) lower than the fully antiferromagnetic ones (the total energy difference between ferromagnetic and antiferromagnetic configurations has been corrected to account for the use of a single determinant in DFT, as discussed below). The nonmagnetic (closed shell singlet) state has an energy 0.22 eV per unit cell higher than the ferromagnetic state (we found a similar value of 0.17 eV per unit cell at the B3PW91 optimized structure, which shows that our conclusion on the magnetization of IrO$_2$ is independent of the choice of the experimental structure). Therefore, we can conclude that the B3PW91 hybrid functional leads to a ferromagnetic ground state for IrO$_2$.

To understand the sensitivity of our results to the amount of exact exchange (EXX), we also performed calculations using

the functional PBE0, which has a higher EXX percentage (25%) than B3PW91 (20%). We found that, for PBE0, the ferromagnetic ground state is lower in energy than the nonmagnetic configuration by 0.42 eV, compared with 0.22 eV at the B3PW91 level of theory (see Table 3). The unpaired spin density (SD) in the ferromagnetic configuration increased with increasing the percentage of EXX: with SD = 0 for PBE (0 EXX); SD = 0.52 per Ir atom with B3PW91 (20% EXX), and SD = 0.59 per Ir atom for PBE0 (25% EXX).

To quantify the strength of magnetic coupling in IrO_2, we computed the spin coupling constants and obtained the theoretical Curie temperature as follows. The low-lying excited states of a magnetic material can be generally described by the Heisenberg Hamiltonian: $H_{spin} = -\Sigma_{ij} J_{ij} \vec{S_i} \cdot \vec{S_j}$, where $\vec{S_i}$ and $\vec{S_j}$ are the vector spin operators on sites i and j, and J_{ij} is the spin coupling constant between $\vec{S_i}$ and $\vec{S_j}$. To obtain the J_{ij} values, we carried out DFT calculations with various distributions of local spins as shown in Table 2. However, since within unrestricted DFT the wave function is represented by a single Slater determinant, it will provide a proper spin state only for closed shell configurations (all orbitals doubly occupied) or for high spin ferromagnetic configurations (all orbitals singly occupied with the same spin). For other cases, we can estimate the energy of the proper singlet spin state following ref 34, under the assumptions that the overlap between two singly occupied orbitals is small. In this case, the single determinant value can be expressed as $J = [(2(E_{s'} - E_T))/(1 + S_{ab})]$, where $E_{s'}$ and E_T are the total energies of antiferromagnetic and ferromagnetic states obtained from DFT, and S_{ab} is the overlap between two singly occupied orbitals. The overlap S_{ab} is approximately zero in the case of IrO_2 and therefore $J \approx 2(E_{s'} - E_T)$. After obtaining the energy difference between ferro- and antiferromagnetic configurations with the proper spin symmetry, we computed the spin coupling constants J (details see in SI), as shown in Tables 2 and 3. The definition of different spin couplings is illustrated in Figure 5, where J_1 represents the
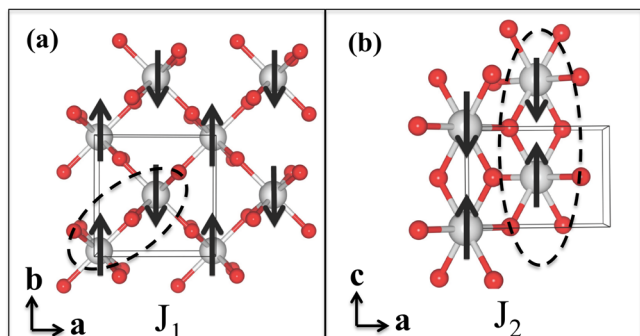
Figure 5. Configurations corresponding to different spin coupling states: J_1, spin coupling between nearest Ir neighboring atoms along the diagonal direction; J_2, spin coupling between repetitions of Ir atoms along the z direction.

coupling between nearest neighbors along the diagonal direction; J_2 represents the spin coupling between repetitions of Ir atom along z. (In these two cases, two Ir atoms interact through the bridging O atoms. We did not consider the interactions between the second nearest neighbors because the magnetic interaction is very weak in this system.) In order to relate to magnetic measurements, we computed the Curie

temperature by using the Brillouin function expression:[35] $T = (2J'\gamma/3k)$, where J' is the spin coupling constant (we considered J' as the exchange coupling between ferromagnetic state and the fully averaged spin state: $J' = J_1 + 1/4J_2$), k is the Boltzmann constant, and γ is given by $S(S + 1)/S^2$ for quantum spins and 1 for classical spins, respectively. It has been found that choosing $\gamma = 1$ improves the agreement between theory and experiment significantly.[36,37] Therefore, we have chosen $\gamma = 1$ in our calculations. It has been shown that the above approximation gives excellent results for the Curie temperature of several metallic systems (with errors less than 10% compared with experimental measurements), for example, Co and NiMn.[38,39] For IrO_2 we found a Curie temperature of 20.4 K (B3PW91) and 32.2 K (PBE0) with an error bar of 2−3 K. The low Curie temperature indicates the magnetic coupling is very weak for this system.

Next we examined the t_{2g} orbitals of IrO_2 obtained by hybrid functionals. Figure 6 shows the PDOS of IrO_2 d states of one Ir
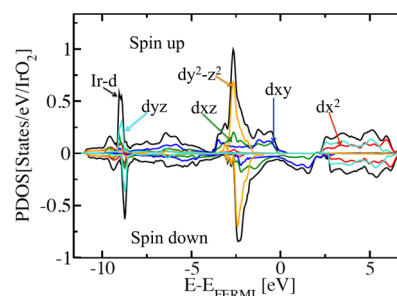
Figure 6. Projected density of states (PDOS) of the 5d states of the central Ir atom of Figure 1 computed with the functional B3PW91: the green and dark blue curves represent the d_{xz} and d_{xy} orbitals, respectively; the light blue curve represents the d_{yz} orbital; and the red and orange curves represent the d_{x^2} and $d_{y^2-z^2}$ orbitals, respectively. The positive and negative PDOS represent spin up and spin down components, respectively.

atom (the axis is defined in the same way as in Figure 3), as obtained by B3PW91. Again the Fermi level crosses the d_{xz} and d_{xy} orbitals, similar to the results obtained at the PBE level; however, for the majority spins (spin up in Figure 6) d_{xz} and d_{xy} orbitals are all occupied below the Fermi level, while for the minority spins (spin down in Figure 6) d_{xz} and d_{xy} orbitals are partially occupied (and the t_{2g} hole is mainly distributed on d_{xy} orbital, as discussed in DFT Description of the Electronic Structure of IrO_2) and positioned above the Fermi level, yielding an overall ferromagnetic character.

Figure 7a shows the comparison of computed DOS obtained with PBE0 and B3PW91 (aligned by their corresponding Fermi levels): below the Fermi level, the PBE0 DOS is systematically shifted to lower energies by 0.2 eV, compared to that of B3PW91; instead, above the Fermi level, the PBE0 DOS is systematically shifted to higher energies by 0.3 eV. The occupied and unoccupied t_{2g} orbitals around the Fermi level are split further apart with PBE0, and the occupation of unpaired d electron is increased, compared to B3PW91 (see Table 3). However, the shape of the DOS is similar to the two functionals.

A comparison between the experimental XPS and the DOS computed within B3PW91 is shown in Figure 7b: all computed peaks are shifted down by 0.5−1 eV compared with the experimental XPS spectrum. We note that XPS data could be sensitive to the surface condition in the measurements, for
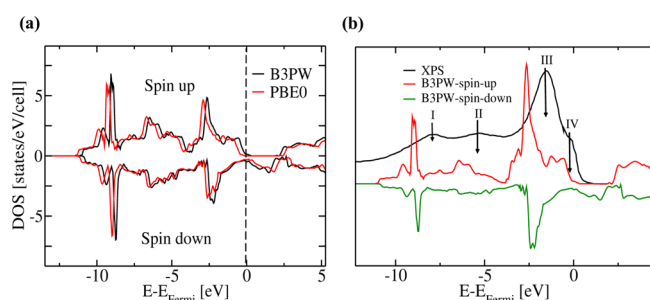
E

Figure 7. Density of states (left) obtained with the B3PW91 (black curve) and PBE0 (red curve) functionals; the density of states (DOS) computed with B3PW91(red and green curves) is compared with the experimental XPS data[40] (black curve) on the right-hand side. The positive and negative DOS represents spin up and spin down components, respectively.

example, to surface dipoles. Surface dipoles can possibly shift the work function of metallic surfaces; however, the positions of states relative to the Fermi level should not change in the presence of the surface dipoles. The systematically downward shifts obtained with B3PW91 is due to the redistribution of density of states of t_{2g} orbitals around the Fermi level; the same redistribution is responsible for the differences between PBE0 and B3PW91 discussed earlier.

◼ DISCUSSIONS

For transition metal oxides such as IrO_2 in which the formal oxidation states leave occupied d electrons (5 for IrO_2), the competition between delocalization to minimize kinetic energy (increasing d conduction bandwidth) and local intra-atomic electron−electron repulsion determines whether the system is metallic or insulating. For late 3d transition metal oxides, the spatial extension of d orbitals is small compared to metal-O bond distances and, therefore, d−d orbital overlaps are small, leading to narrow d bands, for example, ∼1 eV for NiO and ∼3 eV for TiO_2. For FeO, CoO, and NiO, the intra-atomic electron repulsion competes significantly with the band properties, the itinerant properties of the metal break down and electrons become localized to form a Mott insulator. For these strongly correlated Mott insulators, the standard GGA/LDA flavor of DFT leads to an excessive delocalization of the electrons and thus to a metallic ground state. Instead hybrid functional and DFT with Hubbard U correction can capture the correct electron correlation, at least qualitatively, and recover the insulating ground states observed experimentally. It has been shown that for MnO, FeO, CoO, and NiO[41] hybrid functionals and DFT with Hubbard U give similar results for magnetic properties, and the same trend on the band gaps of 3d transition metal oxides. In contrast, for IrO_2, the size of the spatial extension of the Ir valence 5d orbitals is comparable to the Ir−O bond distances so that d−d overlaps are much larger, leading to wider d conduction bandwidth (7.5 eV) than those found in 3d transition metal oxides and much more delocalized d electrons. Hence, applying a Hubbard U correction to increase d electron on-site repulsion of IrO_2 is not as important as for 3d transition metal oxides. Indeed, our results show that, for both zero and finite U, the system is metallic with zero magnetization.

On the other hand, for simple metals, hybrid functionals tend to overestimate bandwidths compared with LDA/GGA, for example, for Na and Al.[17] Also, hybrid functionals tend to

overestimate the magnetic moments for metals, for example, Fe (experiment and PBE both yield 2.2 μ_B, compared to 2.7 μ_B for the HSE functional[17]). One way to interpret the performance of hybrid functionals is to consider the screening properties of the system: the optimal amount of EXX included in the hybrid functionals for each system has been shown to be inversely proportional to the dielectric constant,[16] which should be effectively zero for metals. Local functionals, for example, LDA are derived from the homogeneous electron gas, whose screening properties resemble those of simple metallic systems, for example, Na or Li. The inclusion of the exact exchange in hybrid functionals stabilizes unpaired electrons compared with local/semilocal functionals, and such stabilization could be the source of the overestimation of magnetic moments in several metals.

However, IrO_2 exhibits significant hybridization between O 2p and Ir 5d states which can hardly be described by homogeneous metallic screening. Hence, using hybrid functionals for IrO_2 is better justified than for simple metals. The major difference between PBE and hybrid functional results is that PBE predicts a nonmagnetic ground state, whereas hybrid functionals predict a ferromagnetic ground state with a very weak magnetic coupling. To settle this issue of magnetization in the ground state of IrO_2, we suggest magnetic measurement as a function of temperature down to 5 K.

It is interesting to compare IrO_2 with RuO_2, which also exhibits the rutile crystal structure. Both oxides show good OER catalytic properties. We expect some differences, since RuO_2 has four electrons distributed over the three t_{2g} orbitals leading to a local triplet, with the d_{xy} and d_{xz} orbitals singly occupied. Since the singly occupied orbitals of two neighboring Ru atoms can overlap, we would expect weak superexchange coupling through the intervening oxygen atoms. However, the strong on-site triplet pairing of the two d orbitals weakens the interatomic spin coupling of the antiferromagnetic state by a factor of 2. Again, we would expect fairly narrow t_{2g} bands around the Fermi energy leading to a 2/3 filled set of t_{2g} bands. Previous theoretical calculations of bulk RuO_2 were performed by local or semilocal functionals and obtained a nonmagnetic ground state.[9,10] However, a magnetic ground state was reported for the RuO_2 (110) surface using a DFT-GGA functional.[42] We also obtained a nonmagnetic ground state for bulk RuO_2 by using the PBE functional. However, using the B3PW91 hybrid functional, we found an antiferromagnetic ground state (the same spin configuration as case 2 in Table 2), 0.40 eV/0.90 eV lower than the nonmagnetic/ferromagnetic state from DFT calculation (for a unit cell with two RuO_2 formula). As discussed before, unrestricted DFT can not provide the proper AFM spin state for RuO_2 due to the single Slater determinant of wave functions. At variance from IrO_2, RuO_2 has a local triplet with two unpaired electrons for each Ru atom. We derived the expression for the corrected energy difference between FM and AFM state of RuO_2 (as shown in SI), which is approximately 3/2 times the value from DFT. We have also computed the corrected energy difference between FM and several AFM configurations in Table 4, similar to Table 2. We obtained J_1 −169.0 meV and J_2 −93.8 meV for RuO_2 using the same convention as in Table 3 that is negative for antiferromagnetic coupling and positive for ferromagnetic coupling. Clearly, the magnetic coupling is much stronger for RuO_2 compared with IrO_2. Although RuO_2 is often considered nonmagnetic,[19] Ru−Ru antiferromagnetic interactions have been observed experimentally in nanoparticle RuO_2.[43] These

Table 4. Total Energy Differences between Ferromagnetic and Nonmagnetic (FM-NM) States of RuO_2 Computed with a $2 \times 2 \times 2$ Supercell; Relative Energies (ΔE) between the FM State and Various AFM Configurations[a]

theory	FM-NM (Ha)	ΔE (Ha)			J (meV)	
		2	3	4	J_1	J_2
B3PW	−0.1170	0.3977	0.2672	0.3775	−169.0	−93.8

[a]Configurations 2, 3, and 4 similar to Table 2 of IrO_2 and various spin coupling constants J_1 and J_2 with the same definition as Table 3. The energy components (ΔE) for each spin configuration are based on the formula discussed in the main text and SI.

calculations should stimulate experiments to clarify further whether the magnetic ordering is possible for RuO_2.

CONCLUSION

We studied the electronic structure of IrO_2 at several levels of theory beyond standard LDA/GGA. We found that the electronic states and magnetic properties of IrO_2 are determined by the partial occupation of the t_{2g} orbitals near the Fermi level. All levels of theory, including PBE, PBE with Hubbard correction U (PBE+U), and hybrid functionals (B3PW91 and PBE0), predict a metallic character for bulk IrO_2. However, PBE and PBE+U predict a nonmagnetic ground state, whereas the hybrid functionals predict a ferromagnetic ground state with a very weak magnetic coupling (the predicted Curie temperature is 20 K at B3PW91 and 32 K at PBE0). The best comparison with the experimental XPS spectra was obtained at the PBE level of theory.

ASSOCIATED CONTENT

Ⓢ Supporting Information

The information for local basis sets, the comparison of the structural and electronic properties and phonon frequencies of IrO_2 obtained with the Quantum Espresso package and the Crystal code, the spin coupling constants derivation for RuO_2. The Supporting Information is available free of charge on the ACS Publications website at DOI: 10.1021/acs.jpcc.5b00861.

AUTHOR INFORMATION

Corresponding Authors
*E-mail: wag@wag.caltech.edu.
*E-mail: yping@lbl.gov.

Notes
The authors declare no competing financial interest.

ACKNOWLEDGMENTS

REFERENCES

(1) Spurgeon, J. M.; Velazquez, J. M.; McDowell, M. T. Improving O_2 Production of WO_3 Photoanodes with IrO_2 in Acidic Aqueous Electrolyte. *Phys. Chem. Chem. Phys.* **2014**, *16*, 3623−3631.

(2) McCrory, C. C. L.; Jung, S.; Peters, J. C.; Jaramillo, T. F. Benchmarking Heterogeneous Electrocatalysts for the Oxygen Evolution Reaction. *J. Am. Chem. Soc.* **2013**, *135*, 16977−16987.

(3) Moon, S. J.; Jin, H.; Kim, K. W.; Choi, W. S.; Lee, Y. S.; Yu, J.; Cao, G.; Sumi, A.; Funakubo, H.; Bernhard, C.; et al. Dimensionality-Controlled Insulator-Metal Transition and Correlated Metallic State in $5d$ Transition Metal Oxides $Sr_{n+1}Ir_nO_{3n+1}$ ($n = 1, 2,$ and ∞). *Phys. Rev. Lett.* **2008**, *101*, 226402.

(4) Kim, B. J.; Jin, H.; Moon, S. J.; Kim, J.-Y.; Park, B.-G.; Leem, C. S.; Yu, J.; Noh, T. W.; Kim, C.; Oh, S.-J.; et al. Novel J_{eff} = 1/2 Mott State Induced by Relativistic Spin-Orbit Coupling in Sr_2IrO_4. *Phys. Rev. Lett.* **2008**, *101*, 076402.

(5) Cao, G.; Crow, J.; Guertin, R.; Henning, P.; Homes, C.; Strongin, M.; Basov, D.; Lochner, E. Charge Density Wave Formation Accompanying Ferromagnetic Ordering in Quasi-One-Dimensional $BaIrO_3$. *Solid State Commun.* **2000**, *113*, 657−662.

(6) Cao, G.; Lin, X. N.; Chikara, S.; Durairaj, V.; Elhami, E. High-Temperature Weak Ferromagnetism on the Verge of a Metallic State: Impact of Dilute Sr Doping on $BaIrO_3$. *Phys. Rev. B* **2004**, *69*, 174418.

(7) Maiti, K.; Singh, R. S.; Medicherla, V. R. R.; Rayaprol, S.; Sampathkumaran, E. V. Origin of Charge Density Wave Formation in Insulators from a High Resolution Photoemission Study of $BaIrO_3$. *Phys. Rev. Lett.* **2005**, *95*, 016404.

(8) Cao, G.; Xin, Y.; Alexander, C. S.; Crow, J. E.; Schlottmann, P.; Crawford, M. K.; Harlow, R. L.; Marshall, W. Anomalous Magnetic and Transport Behavior in the Magnetic Insulator $Sr_3Ir_2O_7$. *Phys. Rev. B* **2002**, *66*, 214412.

(9) Xu, J.; Jarlborg, T.; Freeman, A. Self-Consistent Band Structure of the Rutile Dioxides NbO_2, RuO_2, and IrO_2. *Phys. Rev. B* **1989**, *40*, 7939−7947.

(10) de Almeida, J.; Ahuja, R. Electronic and Optical Properties of RuO_2 and IrO_2. *Phys. Rev. B* **2006**, *73*, 165102.

(11) Kahk, J. M.; Poll, C. G.; Oropeza, F. E.; Ablett, J. M.; Céolin, D.; Rueff, J.-P.; Agrestini, S.; Utsumi, Y.; Tsuei, K. D.; Liao, Y. F.; et al. Understanding the Electronic Structure of IrO_2 Using Hard-X-ray Photoelectron Spectroscopy and Density-Functional Theory. *Phys. Rev. Lett.* **2014**, *112*, 117601.

(12) Yang, W.; Cohen, A. J.; Mori-Sánchez, P. Derivative Discontinuity, Bandgap and Lowest Unoccupied Molecular Orbital in Density Functional Theory. *J. Chem. Phys.* **2012**, *136*, 204111.

(13) Mori-Sánchez, P.; Cohen, A. J.; Yang, W. Localization and Delocalization Errors in Density Functional Theory and Implications for Band-Gap Prediction. *Phys. Rev. Lett.* **2008**, *100*, 146401.

(14) Becke, A. D. Density Functional Thermochemistry. III. The Role of Exact Exchange. *J. Chem. Phys.* **1993**, *98*, 5648−5652.

(15) Adamo, C.; Barone, V. Toward Reliable Density Functional Methods without Adjustable Parameters: The PBE0 Model. *J. Chem. Phys.* **1999**, *110*, 6158−6170.

(16) Skone, J. H.; Govoni, M.; Galli, G. Self-Consistent Hybrid Functional for Condensed Systems. *Phys. Rev. B* **2014**, *89*, 195112.

(17) Paier, J.; Marsman, M.; Hummer, K.; Kresse, G.; Gerber, I. C.; Ángyán, J. G. Screened Hybrid Density Functionals Applied to Solids. *J. Chem. Phys.* **2006**, *124*, 154709.

(18) Xiao, H.; Tahir-Kheli, J.; Goddard, W. A. Accurate Band Gaps for Semiconductors from Density Functional Theory. *J. Phys. Chem. Lett.* **2011**, *2*, 212−217.

(19) Ryden, W. D.; Lawson, A. W. Magnetic Susceptibility of IrO_2 and RuO_2. *J. Chem. Phys.* **1970**, *52*, 6058−6061.

(20) Giannozzi, P.; Baroni, S.; Bonini, N.; Calandra, M.; Car, R.; Cavazzoni, C.; Ceresoli, D.; Chiarotti, G. L.; Cococcioni, M.; Dabo, I.; et al. QUANTUM ESPRESSO: A Modular and Open-Source Software Project for Quantum Simulations of Materials. *J. Phys.: Condens. Matter* **2009**, *21*, 395502.

(21) Garrity, K. F.; Bennett, J. W.; Rabe, K. M.; Vanderbilt, D. Pseudopotentials for High-Throughput DFT Calculations. *Comput. Mater. Sci.* **2014**, *81*, 446−452.

(22) Marzari, N.; Vanderbilt, D.; De Vita, A.; Payne, M. C. Thermal Contraction and Disordering of the Al(110) Surface. *Phys. Rev. Lett.* **1999**, *82*, 3296−3299.

(23) Wadt, W. R.; Hay, P. J. Ab Initio Effective Core Potentials for Molecular Calculations. Potentials for Main Group Elements Na to Bi. *J. Chem. Phys.* **1985**, *82*, 284−298.

(24) Roy, L. E.; Hay, P. J.; Martin, R. L. Revised Basis Sets for the LANL Effective Core Potentials. *J. Chem. Theory Comput.* **2008**, *4*, 1029−1031.

(25) Masys, S.; Jonauskas, V.; Grebinskij, S.; Mickevicius, S.; Pakstas, V.; Senulis, M. Theoretical and Experimental Study Of Non-Stoichiometric $SrRuO_3$: A Role of Oxygen Vacancies in Electron Correlation Effects. *Lith. J. Phys.* **2013**, *53*, 150.

(26) Schaefer, H. F. *Methods of Electronic Structure Theory*; Plenum Press: New York, 1977.

(27) McDaniel, C. L.; Schneider, S. J. Phase Relations in the Systems TiO_2−IrO_2 and SnO_2−IrO_2 in Air. *J. Res. Natl. Bur. Stand.* **1967**, *71*, 119.

(28) Jin, H.; Jeong, H.; Ozaki, T.; Yu, J. Anisotropic Exchange Interactions of Spin-Orbit-Integrated States in Sr_2IrO_4. *Phys. Rev. B* **2009**, *80*, 075112.

(29) Jiang, H.; Gomez-Abal, R. I.; Rinke, P.; Scheffler, M. First-Principles Modeling of Localized *d* States with the GW@LDA+U Approach. *Phys. Rev. B* **2010**, *82*, 045108.

(30) Anisimov, V. I.; Aryasetiawan, F.; Lichtenstein, A. I. First-Principles Calculations of the Electronic Structure and Spectra of Strongly Correlated Systems: the LDA+U Method. *J. Phys.: Condens. Matter* **1997**, *9*, 767.

(31) Kang, W.; Hybertsen, M. S. Quasiparticle and Optical Properties of Rutile and Anatase TiO_2. *Phys. Rev. B* **2010**, *82*, 085203.

(32) Cococcioni, M.; de Gironcoli, S. Linear Response Approach to the Calculation of the Effective Interaction Parameters in the LDA+U Method. *Phys. Rev. B* **2005**, *71*, 035105.

(33) Dovesi, R.; Saunders, V. R.; Roetti, C.; Orlando, R.; Zicovich-Wilson, C. M.; Pascale, F.; Civalleri, B.; Doll, K.; Harrison, N. M.; Bush, I. J.; et al. *CRYSTAL09 User's Manual*; Universita di Torino, Torino, Italy, 2009.

(34) Cheng, M.-J.; Nielsen, R. J.; Tahir-Kheli, J.; Goddard, W. A., III The Magnetic and Electronic Structure of Vanadyl Pyrophosphate from Density Functional Theory. *Phys. Chem. Chem. Phys.* **2011**, *13*, 9831−9838.

(35) Kei, Y. *Theory of Magnetism*; Sprinter-Verlag Berlin Heidelberg: New York, 1996.

(36) Liechtenstein, A.; Katsnelson, M.; Antropov, V.; Gubanov, V. Local Spin Density Functional Approach to the Theory of Exchange Interactions in Ferromagnetic Metals and Alloys. *J. Magn. Magn. Mater.* **1987**, *67*, 65−74.

(37) Gyorffy, B. L.; Pindor, A. J.; Staunton, J.; Stocks, G. M.; Winter, H. A First-Principles Theory of Ferromagnetic Phase Transitions in Metals. *J. Phys. F: Met. Phys.* **1985**, *15*, 1337.

(38) Schulthess, T. C.; Butler, W. H. First-Principles Exchange Interactions between Ferromagnetic and Antiferromagnetic Films: Co on NiMn, a Case Study. *J. Appl. Phys.* **1998**, *83*.

(39) MacLaren, J. M.; Schulthess, T. C.; Butler, W. H.; Sutton, R.; McHenry, M. Electronic Structure, Exchange Interactions, and Curie Temperature of FeCo *J. Appl. Phys.* **1999**, *85*.

(40) Riga, J.; Tenret-Noël, C.; Pireaux, J. J.; Caudano, R.; Verbist, J. J.; Gobillon, Y. Electronic Structure of Rutile Oxides TiO_2, RuO_2, and IrO_2 Studied by X-ray Photoelectron Spectroscopy. *Phys. Scr.* **1977**, *16*, 351.

(41) Tran, F.; Blaha, P.; Schwarz, K.; Novák, P. Hybrid Exchange-Correlation Energy Functionals for Strongly Correlated Electrons: Applications to Transition-Metal Monoxides. *Phys. Rev. B* **2006**, *74*, 155108.

(42) Torun, E.; Fang, C. M.; de Wijs, G. A.; de Groot, R. A. Role of Magnetism in Catalysis: RuO_2 (110) Surface. *J. Phys. Chem. C* **2013**, *117*, 6353−6357.

(43) Diaz, C.; Valenzuela, M.; Spodine, E.; Moreno, Y.; Pena, O. A Cyclic and Polymeric Phosphazene as Solid State Template for the Formation of RuO_2 Nanoparticles. *J. Cluster Sci.* **2007**, *18*, 831−844.